Materials Research. 2019; v22(suppl. 1): e20180862
DOI: http://dx.doi.org/10.1590/1980-5373-MR-2018-0862

Influence of the Treatment Time on the Surface Chemistry and Corrosion Behavior of Cerium-Based Conversion Coatings on the AZ91D Magnesium Alloy

***Eloana Patrícia Ribeiro*[a]*, *Antonio Augusto Couto*[a], *Leandro Antonio de Oliveira*[b], *Renato Altobelli Antunes*[b]**

[a] *Instituto de Pesquisas Energéticas e Nucleares (IPEN), Centro de Ciência e Tecnologia de Materiais (CCTM), São Paulo, SP, Brasil*
[b] *Universidade Federal do ABC (UFABC), Centro de Engenharia, Modelagem e Ciências Sociais Aplicadas (CECS), Santo André, SP, Brasil*

Received: December 08, 2018; Revised: November 04, 2019; Accepted: November 25, 2019.

The aim of the present work was to investigate the effect of the treatment time on the surface chemistry and corrosion behavior of cerium-based chemical conversion coatings on the AZ91D magnesium alloy. The conversion coating was prepared by the immersion technique from a bath consisting of 0.05 mol.L^{-1} $Ce(NO_3)_3.6H_2O$ and 0.254 mol.L^{-1} H_2O_2 (30 wt.%) for times ranging from 20 s to 120 s. The surface chemistry was examined by X-ray photoelectron spectroscopy (XPS). The corrosion behavior was assessed by electrochemical impedance spectroscopy and potentiodynamic polarization. XPS analysis detected the presence of cerium oxides (Ce_2O_3 and CeO_2) and cerium/magnesium hydroxides. The best corrosion behavior was observed for the treatment conducted for 60 s. The results are discussed with respect to coating morphology and composition.

Keywords: *AZ91D alloy, cerium conversion coating, XPS, corrosion.*

1. Introduction

Magnesium alloys are the most attractive metallic materials for technological application in lightweight structures, owing to their low density (approximately 1,7 g/cm^3)[1, 2] and high strength-to-weight ratio[3]. Additionally, Mg presents biocompatibility, non-toxicity and is recyclable[2]. One major limitation for the widespread use of magnesium-based structural components is its intrinsic high chemical reactivity[4-15]. The AZ series is an alloying system for magnesium alloys having aluminum (2-10 wt.%) and zinc as the main alloying elements[16].

The corrosion resistance of magnesium alloys with cerium-based conversion coatings has been evaluated by several authors[17-20]. Protective coatings have been developed in order to overcome this limiting design feature of magnesium alloys. Different deposition methods may be employed such as electrodeposition, physical vapor deposition, anodization and chemical conversion coatings[1]. The conversion process is usually conducted by immersion at temperatures below 50°C in the presence of an oxidant, resulting in the formation of hydrated species or mixed oxides[21].

Chromates based conversion coating has good efficiency, but its toxicity has led to legislation restrictions, driving the development of non-aggressive treatments[5]. Cerium-based conversion coatings have gained growing interest in the corrosion control of magnesium alloys. Rare-earth elements act as cathodic inhibitors. Cerium is the most active of the rare-earth elements. The corrosion resistance follows the order Ce>Nd>Pr>Y>La[21]. The main action mechanism of rare earth elements is by the precipitation of oxides/hidroxides on substrate cathodic regions. Coating integrity and thickness determine its protection. Some cracks appear in the rare earth-based conversion coatings[21-23].

It is generally agreed that coating morphology has a marked influence on the overall protection ability of the converted surface film. Moreover, surface chemistry is also an important issue. X-ray photoelectron spectroscopy (XPS) is frequently used to examine the chemical composition of cerium conversion films[15, 18, 24-28]. It provides unique information regarding the chemical states of different species that constitute the converted layer. Cerium compounds can be found in two different oxidation states, namely Ce^{4+} and Ce^{3+} [24, 25]. The treatment time can be varied to tailor the atomic fraction of each one of these components in the conversion layer. The corrosion behavior of the treated substrate is, therefore, affected by this parameter.

The aim of this work was to investigate the effect of the treatment time on the corrosion behavior of cerium-based conversion coatings developed on the AZ91D magnesium alloy. The correlation between the surface chemistry of the converted layers, their morphology and corrosion resistance is examined.

2. Experimental

2.1 Materials, surface preparation and conversion coating procedure

The AZ91D ingot was kindly provided by Rima Industrial Magnésio S/A (Brazil). It was produced by die-casting and

*e-mail: eloana.ribeiro@gmail.com

was used in the as-received state. Its nominal chemical composition is shown in Table 1. Specimens were cut from the ingot using silicon carbide blades, thus obtaining pieces with approximately 7 x 6 x 5 mm. Next, the specimens were connected to a copper wire using colloidal silver paste, followed by embedding in cold curing epoxy resin. After curing, the specimens were mechanically ground using silicon carbide emery papers up to 2400 grit. The final surface finishing step was polishing by diamond paste (6 μm), being subsequently, degreased with ethanol, rinsed in deionized water and dried under a warm air stream provided by a conventional heat gun.

The conversion coatings were prepared by immersing the specimens in a solution consisting of 0.05 mol.L^{-1} $Ce(NO_3)_3.6H_2O$ and 0.254 mol.L^{-1} H_2O_2. The treatment was carried out at room temperature for different times: 20 s, 60 s and 120 s. After immersion, the specimens were rinsed in deionized water and let dry at open air.

2.2 Characterization

Coating morphology was examined by confocal laser scanning microscopy (CLSM - Olympus LEXT OLS4100 instrument) and scanning electron microscopy (SEM – FEI Quanta 250). The surface chemistry of the converted films was analyzed by energy dispersive spectroscopy (EDS - JEOL JSM- 6010LA) and X-ray photoelectron spectroscopy (XPS) using a ThermoFisher Scientific K-alpha$^+$ spectrometer operating with Al-kα radiation source. The chemical states for Ce3d and O1s were identified by analyzing the binding energies calibrated to that of C1s peak (adventitious carbon) at 284.8 eV. The spectra were curve-fitted using the Avantage™ software and background subtraction by the Smart algorithm. The coating thickness was analysed by surface profilometry (KLA – Tencor model P7).

The corrosion behavior was assessed by electrochemical impedance spectroscopy (EIS) and potentiodynamic polarization. All tests were carried out using a potentiostat/galvanostat Autolab M101. A conventional three-electrode cell configuration was employed with a platinum wire as the counter-electrode, Ag/AgCl as reference and the AZ91D samples as the working electrodes. Initially, the open circuit potential was monitored for 1 h. Next, EIS measurements were performed at the open circuit potential in the frequency range from 100 kHz to 10 mHz with an amplitude of the perturbation signal of ±10 mV (rms) and an acquisition rate of 10 points per decade. Then, the samples were subjected to potentiodynamic polarization from – 300 mV with respect to the open circuit potential up to +0.5 $V_{Ag/AgCl}$ at a sweep rate of 1 mV.s^{-1}. The tests were conducted in triplicate.

3. Results and Discussion

3.1 Coating morphology

Figure 1 shows CLSM micrographs of the uncoated and cerium-coated AZ91D alloy. After the conversion treatment, the samples had a good coating coverage and presented a yellow-colored surface, whose intensity was dependent on the treatment time, ranging from soft yellow to a more intense gold-colored aspect for longer periods of immersion. The yellow-colored surface is typical of the presence of Ce^{4+} on the conversion layers. It scales up with the concentration of this species[21, 29-30]. SEM micrographs show the presence of several cracks and exfoliated regions on the surface film. It is possible to observe the formation of two layers as shown in Figure 2. The outer layer presents several cracks and exfoliated regions. There are also small nodular clusters distributed within it, suggesting the initial stage of a third layer formation. Microcracks and nodular clusters increase with the immersion time, but exfoliation doesn't follow the same process (Figure 3).

Literature presents many possibilities to explain microcracks formation[31]. Wang et al.[29] observed microcracks on the cerium conversion layer formed over the AZ91D alloy. The cracks were mainly concentrated on the α-Mg phase, which promoted a thicker layer growth. This increase of the α-Mg phase thickness can occur because of its lower electrochemical potential with respect to the β phase that induces a preferential deposition region. The different coating growth rates can cause stress generation and microcracks formation[29,32]. Maddela et al.[33, 34] related the microcracks incidence, density, morphology and size with the dimensions of cerium particles and coating thickness. According to these authors, coating homogeneity is due to the cerium oxide particles distribution. Smaller particles result in better homogeneity. Bagalà et al.[35] related microcracks formation with stress generation during drying process, which act as stress relieve mechanism. Besides all presented possibilities for this phenomenon, the better hypothesis, in accordance with other authors, is that the lower electrochemical potential of α-Mg phase, when exposed to the conversion bath, promotes hydrogen evolution around itself, during coating formation. Thus, hydrogen blisters are formed and, when they burst, microcracks and exfoliations can be formed[32,34,36]. It was possible to see hydrogen evolution during the conversion coating formation on the surface of our samples, as showed in Figure 4.

Lee et al.[36] reported H_2 evolution is a common fact during cerium-based conversion coating treatment on magnesium alloys in the presence of H_2O_2. Blisters are formed due to

Table 1. Nominal Chemical composition of the AZ91D alloy (wt.%).

Material	Al	Zn	Mn	Si	Fe	Cu	Ni	Mg
AZ91D	8.3 - 9.7	0.35 – 1.0	0.15 – 0.30	< 0.1	< 0.005	< 0.030	<0.002	Balance

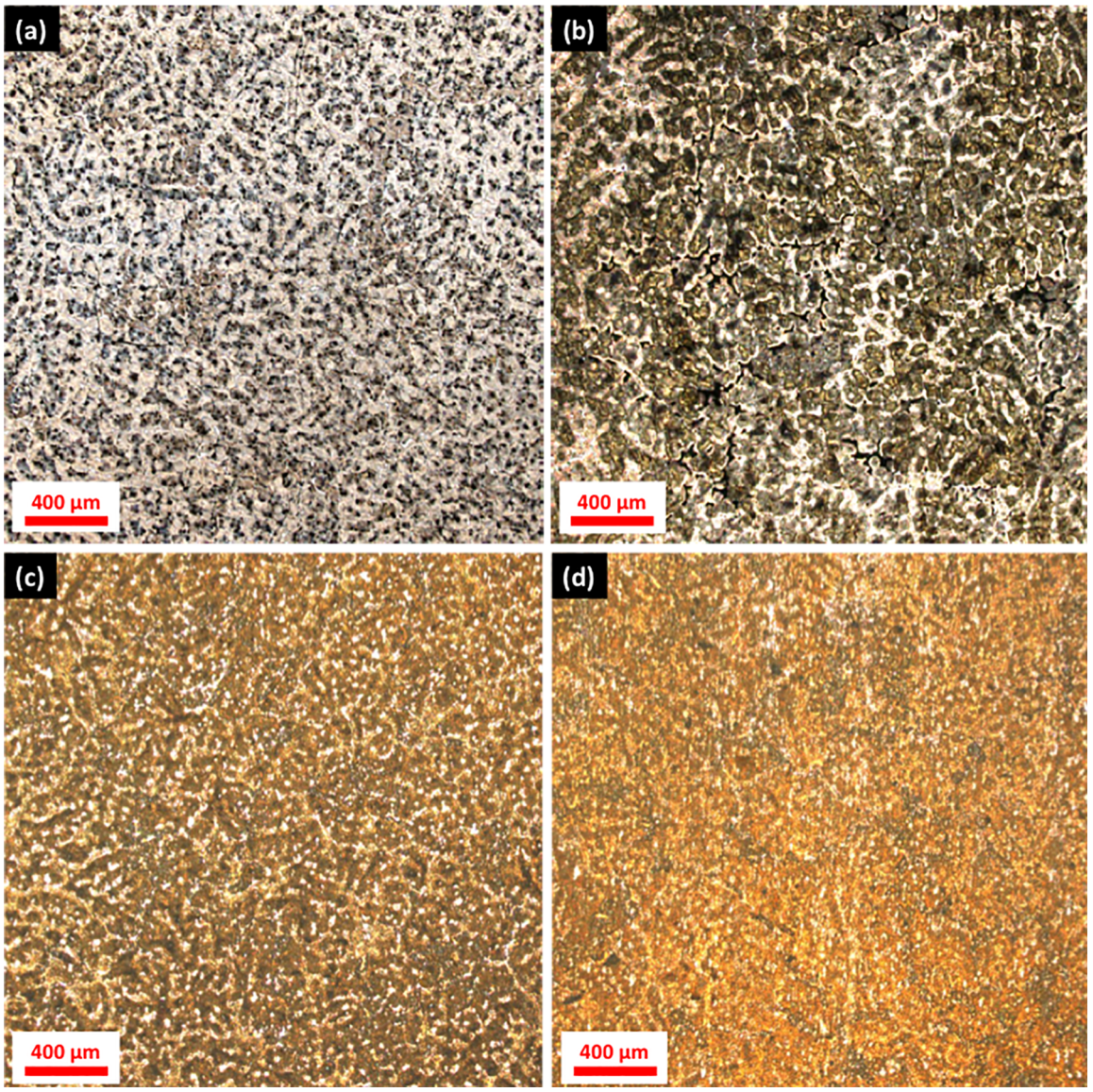

Figure 1. CLSM micrographs for the AZ91D alloy in the a) uncoated and cerium-coated conditions: b) 20 s; c) 60 s and d) 120 s.

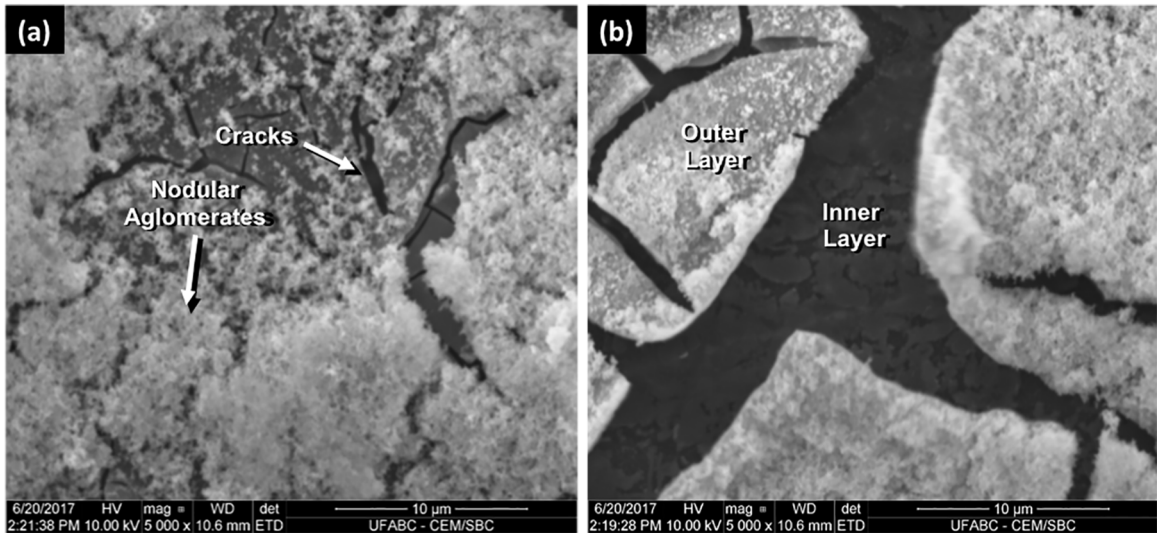

Figure 2. SEM micrographs for the AZ91D alloy in cerium-coated 120 seg.

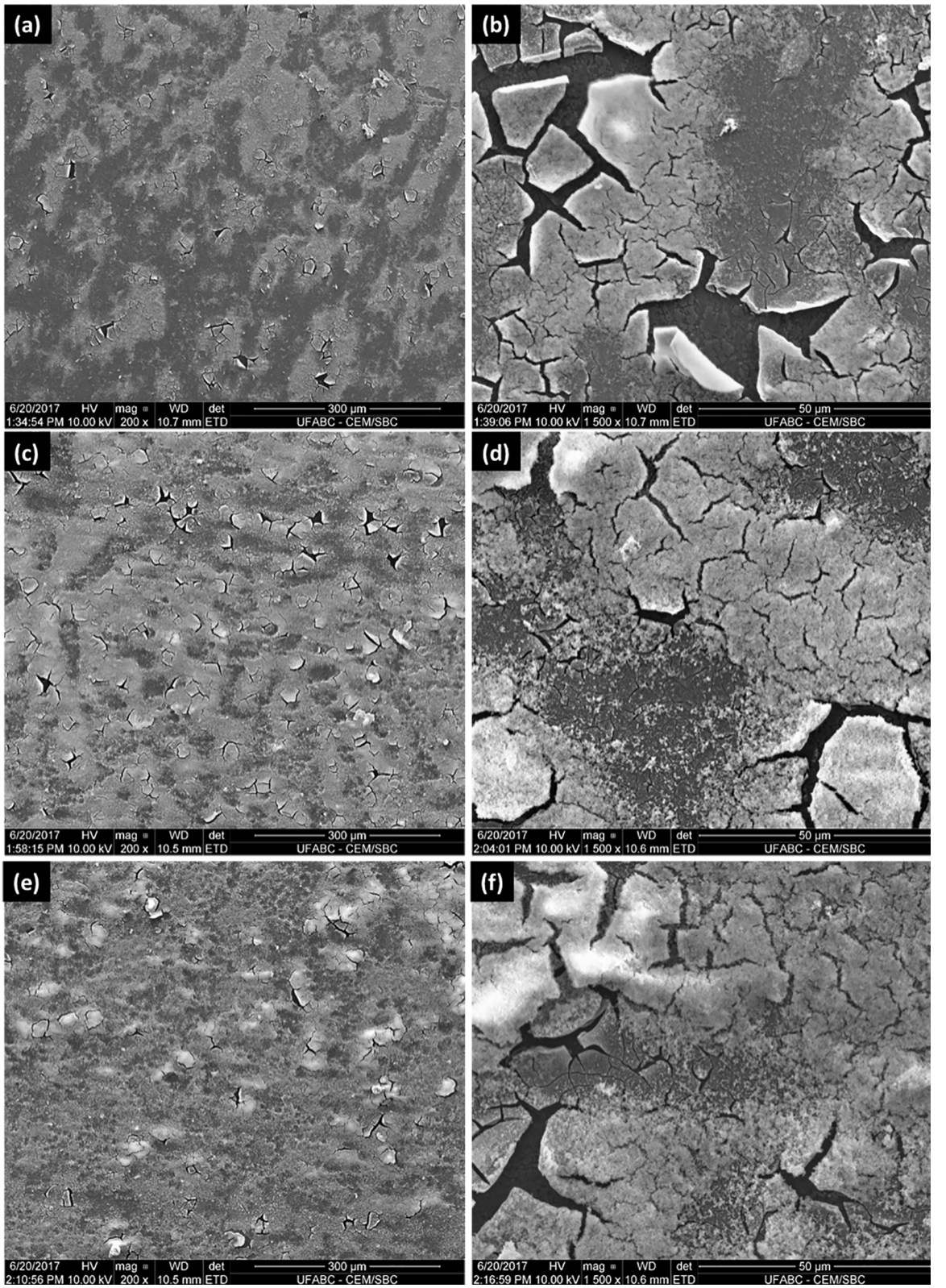

Figure 3. SEM micrographs for the AZ91D alloy in cerium-coated conditions: a) and b) 20 s; c) and d) 60 s; e) and f) 120 s.

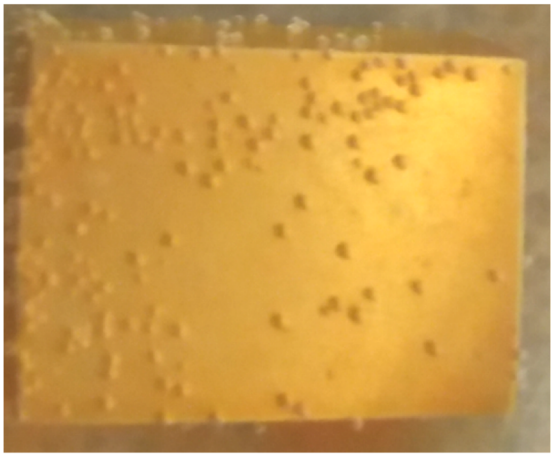

Figure 4. AZ91D alloy during cerium conversion coating bath with hydrogen evolution.

H_2 evolution during metal/coating interface anodic and cathodic reactions. When blisters evolution is more severe some cracks and exfoliation may appear in the top surface. Blisters are mainly formed around α-Mg phase because of the electrochemical potential difference between this phase and the Al-rich β-phase on the AZ91D alloy. Blisters pressure increase during the process and can promote cracks and exfoliations over the α-Mg phase.

EDS maps were acquired to examine the distribution of Ce, Mg and O over the coated surfaces. The results are shown in Figure 5. Oxygen and cerium are the major elements in the coating layer. Magnesium major incidence is at the cracked regions. This signal may arise from both the inner layer of the converted film and from the substrate. Sun et al.[30] reported EDS analysis of the inner layer of cerium conversion coatings on the AZ91D alloy. They have also found Mg and O at this part of the film. Sun et al.[32] reported that the inner layer has MgO in the composition and the outer layer has Ce_2O_3 and CeO_2. The formation of nodular distributed over the outer layer of the coating was also observed by the same authors[30, 32], who showed that they are enriched with Ce.

3.2 Surface chemistry

XPS survey spectra of the cerium-coated AZ91D alloy are shown in Figure 6. Ce3d was detected in all the converted layers, independently of the treatment time, revealing that cerium incorporation was successful. Magnesium and oxygen peaks were also detected. Oxygen is typically associated with the presence of cerium oxides on the conversion coating,

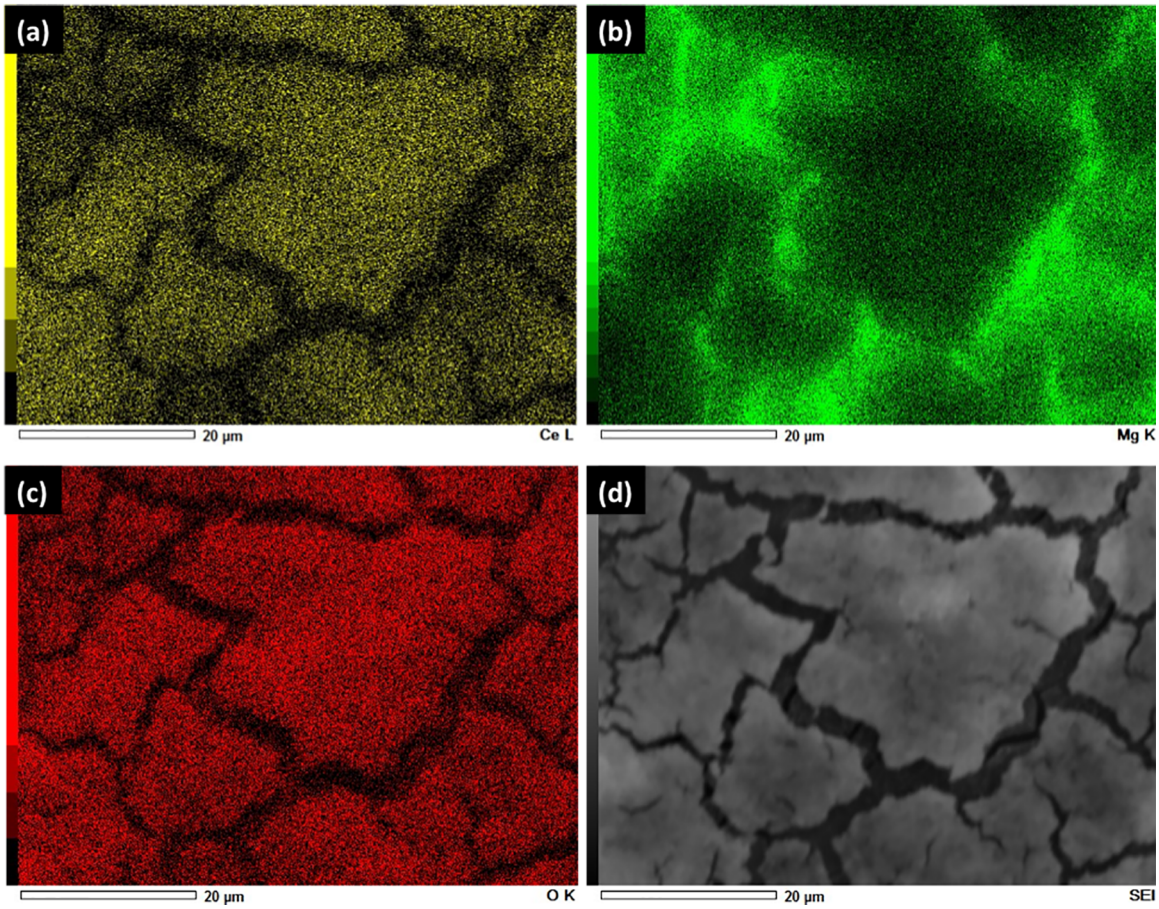

Figure 5. EDX maps for the AZ91D alloy after 60 s of immersion: a) Ce; b) Mg; c) O and d) SEI micrograph.

but can be related to other oxides, like magnesium and/or aluminum oxides. Magnesium can be either part of the converted layer or the signal can also be due to the metallic substrate. The C1s peak was ascribed to surface contamination by hydrocarbons (adventitious carbon).

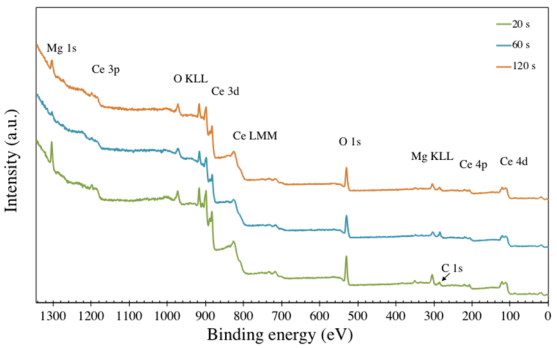

Figure 6. XPS survey spectra of the cerium-coated AZ91D alloy.

XPS core levels for the Ce3d and O1s regions were obtained for the cerium-coated AZ91D alloy. A representative spectrum for each one of these regions is shown in Figure 7 and Figure 8 for the Ce3d and O1s regions of the treated samples. The simultaneous presence of two oxidation states, covalence hybridization effects and spin-orbit splitting make the Ce3d spectrum complex. The covalency hybridization effects imply in the presence of three doublets for the Ce^{4+} oxidation states, designated as v-u, v''-u'' and v'''-u''', and two doublets for the Ce^{3+} oxidation state, designated as v^0-u^0 and v'-u'. A strong spin-orbit splitting is observed for the $3d_{5/2}$ and $3d_{3/2}$ components[24-26].

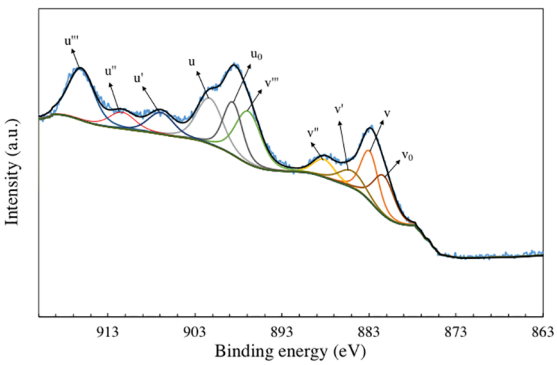

Figure 7. Representative XPS core level for the Ce3d region of the conversion film obtained after 60 s of immersion.

The presence of Ce^{4+} in the conversion coating can be unequivocally indicated by the u''' peak at approximately 916 eV which is normally considered as a fingerprint for this oxidation state, being well isolated from the other peaks and exclusive of Ce^{4+} species[24-26]. Peak fitting allowed calculating the relative area of Ce^{3+} and Ce^{4+} peaks, thus enabling to quantify the ratio of these oxidation states in the conversion layers. The results are shown in Table 2. Ce^{4+} is the major species independently of the treatment time which is associated with the effect of hydrogen peroxide in the conversion bath that promotes oxidation of Ce^{3+} to Ce^{4+}. Ce_2O_3 and CeO_2 presence in the layer indicates that Ce^{4+} and Ce^{3+} contribute to coating formation. The formation of Ce^{4+} is reported to be beneficial to the corrosion resistance of the conversion film due to the passivating effect of CeO_2[25, 26, 37-39]. Considering, though, the intrinsic uncertainty of XPS quantitative analysis[40], it is possible to infer that the Ce^{3+}/Ce^{4+} ratios are very similar for all coatings and the treatment time did not affect it significantly.

The O1s core level is characterized by three components, independently of the immersion time, as shown in Figure 8. The low binding energy component is assigned to CeO_2 whereas the intermediate component is assigned to Ce_2O_3. The highest binding energy component can be due to hydroxide species or adsorbed water[18, 27, 28].

Based on the results obtained by XPS and SEM/EDS analyses and supported by the literature[36], it is possible to suggest a coating formation mechanism for cerium-based conversion coating produced in the present work. It has a layer by layer formation. The composition of the coating in the metal interface mainly consists of MgO as indicated in the EDS maps. The inner layer is followed by layers rich in cerium oxides, as illustrated in Figure 9.

The reactions involved in the conversion coating formation process would be:

$$Mg \rightarrow Mg^{2+} + 2\ e^- \quad (1)$$

$$2\ H_2O + 2\ e^- \rightarrow H_{2(g)} \uparrow + 2\ OH^- \quad (2)$$

$$Mg^{2+} + 2\ OH^- \rightarrow Mg(OH)_{2(s)} \downarrow \quad (3)$$

$$Ce^{3+} + 3\ OH^- \rightarrow Ce(OH)_{3(s)} \downarrow \quad (4)$$

$$Mg(OH)_2 \rightarrow MgO_{(s)} + H_2O \quad (5)$$

$$Ce(OH)_3 \rightarrow Ce_2O_{3(s)} + H_2O \quad (6)$$

$$2\ Ce^{3+} + 2\ OH^- + H_2O_2 \rightarrow 2\ Ce(OH)_2^{2+} \quad (7)$$

$$Ce(OH)_2^{2+} + 2\ OH^- \rightarrow Ce(OH)_{4(s)} \downarrow \quad (8)$$

$$Ce(OH)_4 \rightarrow CeO_{2(s)} + H_2O \quad (9)$$

$$H_2O_2 + 2\ e^- \rightarrow 2\ OH^- \quad (10)$$

Table 2. XPS fitting parameters for the Ce3d core levels of the cerium-coated AZ91D alloy.

Immersion time (s)	v0-u0		v-u		v'-u'		v''-u''		v'''-u'''		Ce^{3+}/Ce^{4+}
	BE (eV)	% at.	BE (eV)	% at.	BE (eV)	% at.	BE (eV)	% at.	BE (eV)	% at.	
20	879.75 - 900.59	18.51	881.97 - 903.24	16.07	883.88 - 906.09	13.92	887.53 - 911.87	13.86	897.43 - 915.85	37.64	0.48
60	881.30 - 898.67	21.96	882.93 - 901.30	24.47	885.01 - 906.90	11.9	888.16 - 911.36	9.54	896.88 - 916.09	32.13	0.51
120	878.68 - 898.57	13.36	881.85 - 900.68	22.61	883.51 - 901.53	18.9	888.16 - 906.90	12.24	897.17 - 916.40	32.89	0.48

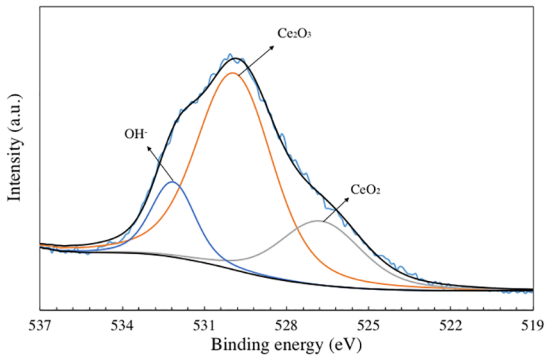

Figure 8. Representative XPS core level for the O1s region of the conversion film obtained after 60 s of immersion.

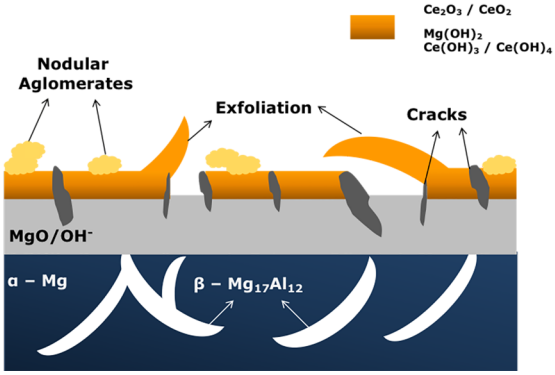

Figure 9. Cerium conversion coating formation illustration.

3.3 Electrochemical behavior

Nyquist plots of the cerium-coated samples are shown in Figure 10. The data were obtained in 3.5 wt.% NaCl solution at room temperature. Magnesium and its alloys are commonly corroded in NaCl solutions, caused by the presence of Cl^- ions and its corrosion susceptibility (reactivity)[3]. The shape of the plots is similar irrespective of the immersion time, being characterized by a capacitive loop in the medium to high frequency domain whose diameter depends on the treatment time. At the lowest frequencies an inductive loop appears which is typical of adsorbed species in magnesium alloys, arising from dissolution of a metallic species, releasing its cation to solution with the formation of an intermediate species such as $Mg(OH)^+_{ads}$ or Mg^+_{ads} [41, 42, 43]. This effect is associated with corrosion processes of the underlying metal and possible initiation of pitting corrosion through defects in the coating layer[44-46]. However, corrosion pits were not detected in the samples subjected to the electrochemical tests. The diameter of the capacitive loop is associated with the corrosion resistance of the electrode, being related to the charge transfer resistance[47, 48]. In this respect, the film obtained at an immersion time of 60 s presented the highest corrosion resistance. The diameter of the capacitive loop presents an increasing trend with the immersion time up to 60 s. This trend is reversed at 120 s, that is, the corrosion resistance was found to decrease when the treatment time increased from 60 s to 120 s. This behavior seems to be related to the surface chemistry of the cerium-based films, as the Ce^{3+}/Ce^{4+} ratios shown in Table 2 correlate with the corrosion resistance as obtained from the EIS measurements.

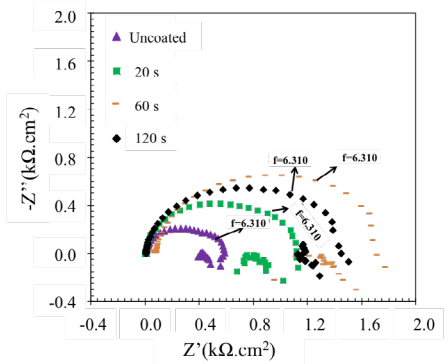

Figure 10. Nyquist plots of the uncoated and cerium-coated AZ91D alloy. Electrolyte: 3.5 wt.% NaCl solution at room temperature.

Potentiodynamic polarization curves of the AZ91D alloy in the as-polished and cerium-coated conditions are shown in Figure 11. The curves were obtained in 3.5 wt.% NaCl solution at room temperature. The values of corrosion potential (E_{corr}) and corrosion current density (i_{corr}) were determined from these curves by the Tafel extrapolation method and are displayed in Table 3. The lowest icorr was obtained for the 60 s condition. This result is in agreement with the EIS measurements. The sample immersed for 60 s presents the highest corrosion potential and the lowest anodic current densities. Coating thickness may affect the corrosion resistance of conversion films[41]. Surface profilometry analyses allowed determining the thickness of the converted layers as 533 nm, 846 nm and 1900 nm for the coatings obtained at 20 s, 60 s, and 120 s, respectively. There is a clear trend of increasing coating thickness as the treatment time increases which is consistent with the literature[41]. Notwithstanding, the corrosion resistance of the thickest film (120 s) was lower than that of the coating obtained at 60 s which, in turn, presented an intermediate thickness. This result suggests that coating thickness may not guarantee a more protective character of the coating against corrosion. Coating integrity can play a dominant role. The presence of more defective surfaces is reported to increase with the treatment time for different types of coatings such as hydroxyapatite layers obtained by dip coating[49] and sputtered cerium oxide films[50] This effect lead to a defective barrier against electrolyte penetration, thus leading to higher corrosion rates when the thicker, defective coating is compared with a more compact and thinner surface. In this respect, coating morphology would be of prime importance to the corrosion behavior of the conversion coatings obtained in the present work.

Additionally, our results pointed to a similar Ce^{3+}/Ce^{4+} ratio for all coatings (Table 2). The influence of the treatment time was, therefore, more significant on the coating morphology and thickness than its surface chemistry. The corrosion behavior was correspondingly more dependent on the morphological features of the converted layer than on its chemical composition.

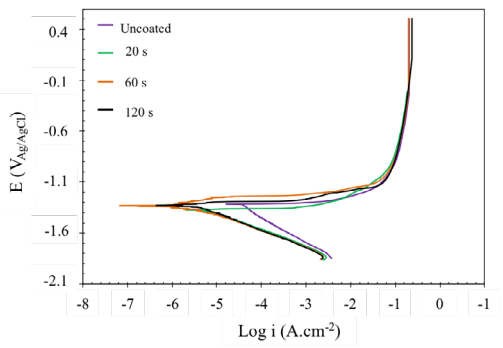

Figure 11. Potentiodynamic polarization curves for uncoated and cerium-coated AZ91D alloy. Electrolyte: 3.5 wt.% NaCl solution at room temperature.

Table 3. Electrochemical parameters determined from the potentiodynamic polarization curves shown in Figure 11.

Immersion time	i_{corr} (μA/cm²)	E_{corr} ($V_{Ag/AgCl}$)
AZ91D	39.2 ± 5.7	- 1.34 ± 0.10
20 s	5.9 ± 0.7	- 1.35 ± 0.02
60 s	1.6 ± 0.7	- 1.26 ± 0.07
120 s	3.9 ± 0.6	- 1.30 ± 0.03

4. Conclusions

The surface chemistry was studied by XPS. The results indicated that Ce^{4+} was the predominant oxidation state in the converted films irrespective of the treatment time. In addition, the coating is formed by two types of layers: an inner layer, for which the composition of the coating at the metal interface mainly consists of MgO, followed by outer layers rich in cerium oxides. The electrochemical behavior of the conversion films was dependent on the treatment time. The best corrosion resistance was observed for the samples that remained 60 s in the conversion bath. It was not possible to identify a clear correlation between the surface chemistry and corrosion resistance. The results suggest that the treatment time affects the electrochemical behavior by increasing the thickness of the converted layer. Notwithstanding, there is an optimum condition at 60 s. For longer immersion times the corrosion resistance decreases which is likely to be associated with the formation of a more defective film.

5. References

1. Fajardo S, Bosch A, Frankel GS. Anomalous hydrogen evolution on AZ31, AZ61 and AZ91 magnesium alloys T in unbuffered sodium chloride solution. *Corrosion Science*. 2019;146:163-171.

2. Esmaily M, Svensson JE, Fajardo S, Birbilis N, Frankel GS, Virtanen S, et al. Fundamentals and advances in magnesium alloy corrosion. *Progress in Materials Science*. 2017;89:92-193.

3. Babilas R, Bajorek A, Simka W, Babilas D. Study on corrosion behavior of Mg-based bulk metallic glasses in NaCl solution. *Electrochimica Acta*. 2016;209:632-642.

4. Liu B, Zhang X, Xiao GY, Lu YP. Phosphate chemical conversion coatings on metallic substrates for biomedical application: a review. *Materials Science and Engineering: C*. 2015;47:97-104.

5. Phuong NV, Lee K, Chang D, Kim M, Lee S, Moon S. Zinc phosphate conversion coatings on magnesium alloys: a review. *Metals and Materials International*. 2013;19(2):273-281.

6. Gray JE, Luan B. Protective coatings on magnesium and its alloys — a critical review. *Journal of Alloys and Compounds*. 2002;336(1-2):88-113.

7. Li L, Qian J, Lu Z, Sun Z. Corrosion mechanism and model of anodized film on AZ91D magnesium alloy. *International Journal of Modern Physics B*. 2010;24(15-16):3077-3082.

8. Fan XL, Huo YF, Li CY, Kannan MB, Chen XB, Guan SK, et al. Corrosion resistance of nanostructured magnesium hydroxide coating on magnesium alloy AZ31: influence

of EDTA. *Rare Metals*. 2019;38(6):520-531. DOI: https://doi.org/10.1007/s12598-019-01216-3

9. Cui XJ, Ning CM, Shang LL, Zhang GA, Liu XQ. Structure and anticorrosion, friction, and wear characteristics of Pure Diamond-Like Carbon (DLC), Cr-DLC, and Cr-H-DLC films on AZ91D Mg alloy. *Journal of Materials Engineering and Performance*. 2019;28:1213.

10. Zhang X, Zhang K, Li XG, Wang C, Li HW, Wang CS, et al. Corrosion and electrochemical behavior of as-cast Mg-5Y-7Gd-1Nd-0.5Zr magnesium alloys in 5% NaCl aqueous solution. *Natural Science: Materials International*. 2011;21(4):314-321.

11. Song J, Cui X, Jin G, Cai Z, Liu E, Li X, et al. Self-healing conversion coating with gelatin–chitosan microcapsules containing inhibitor on AZ91D alloy. *Surface Engineering*. 2018;34(1):79-84.

12. Oktay G, Ürgen M. Corrosion behaviour of magnesium AZ31 sheet produced by twin roll casting. *Corrosion Engineering, Science and Technology*. 2015;50(5):380-389.

13. Song YW, Shan DY, Han E. High corrosion resistance of electroless composite plating coatings on AZ91D magnesium alloys. *Electrochimica Acta*. 2008;53(5):2135-2143.

14. Dai Y, Li Q, Gao H, Li LQ, Chen FN, Luo F, et al. Effects of five additives on electrochemical corrosion behaviours of AZ91D magnesium alloy in sodium chloride solution. *Surface Engineering*. 2011;27:536-543.

15. Feng H, Liu S, Du Y, Lei T, Zeng R, Yuan T. Effect of the second phases on corrosion behavior of the Mg-Al-Zn alloys. *Journal of Alloys and Compounds*. 2017;695:2330-2338.

16. Li Z, Yuan Y, Jing X. Composite coatings prepared by combined plasma electrolytic oxidation and chemical conversion routes on magnesium-lithium alloy. *Journal of Alloys and Compounds*. 2017;706:419-429.

17. Bai LQ, Li D, Guo M, Xin J. Rare earth conversion coating of magnesium alloy AZ91D. *Materials Science Forum*. 2007;546-549:555-558.

18. Castano CE, O'Keefe MJ, Fahrenholtz WG. Microstructural evolution of cerium-based coatings on AZ31 magnesium alloys. *Surface and Coatings Technology*. 2014;246:77-84.

19. Jiang X, Guo R, Jiang S. Microstructure and corrosion resistance of Ce–V conversion coating on AZ31 magnesium alloy. *Applied Surface Science*. 2015;341:166-174.

20. Wang X, Zhub L, Hea X, Sun F. Effect of cerium additive on aluminum-based chemical conversion coating on AZ91D magnesium alloy. *Applied Surface Science*. 2013;280:467-473.

21. Harvey TG. Cerium-based conversion coatings on aluminium alloys: a process review. *Corrosion Engineering, Science and Technology*. 2013;48(4):248-269.

22. Zhang X, Zhong F, Li X, Liu B, Zhang C, Buhe B, et al. The effect of hot extrusion on the microstructure and anti-corrosion performance of LDHs conversion coating on AZ91D magnesium alloy. *Journal of Alloys and Compounds*. 2019;788:756-767.

23. Shoja R, Aghdam ASR. Corrosion of environmentally friendly lanthanum conversion coating on AA2024-T3 aluminum alloy. *Protection of Metals and Physical Chemistry of Surfaces*. 2014;50(1):88-93.

24. Bêche E, Charvin P, Perarnau D, Abanades S, Flamant G. Ce 3d XPS investigation of cerium oxides and mixed cerium oxide ($Ce_xTi_yO_z$). *Surface and Interface Analysis*. 2008;40(3-4):264-267.

25. Uhart A, Ledeuil JB, Gonbeau D, Dupin JC, Bonino JP, Ansart F, et al. An Auger and XPS survey of cerium active corrosion protection forAA2024-T3 aluminum alloy. *Applied Surface Science*. 2016;390:751-759.

26. Sànches-Amaya JM, Blanco G, Garcia-Garcia FJ, Bethencourt M, Botana J. XPS and AES analyses of cerium conversion coatings generated on AA5083 by thermal activation. *Surface and Coatings Technology*. 2012;213:105-116.

27. Lei L, Shi J, Wang X, Liu D, Xu H. Microstructure and electrochemical behavior of cerium conversion coating modified with silane agent on magnesium substrates. *Applied Surface Science*. 2016;376:161-171.

28. Loperena AP, Lehr IL, Saidman SB. Formation of a cerium conversion coating on magnesium alloy using ascorbic acid as additive. Characterization an anticorrosive properties of the formed films. *Journal of Magnesium and Alloys*. 2016;4(4):278-285.

29. Wang C, Zhu S, Jiang F, Wang F. Cerium conversion coatings for AZ91D magnesium alloy in ethanol solution and its corrosion resistance. *Corrosion Science*. 2009;51(12):2916-2923.

30. Sun J, Wang G. Preparation and corrosion resistance of cerium conversion coatings on AZ91D magnesium alloy by a cathodic electrochemical treatment. *Surface and Coatings Technology*. 2014;254:42-48.

31. Arthanari S, Shin KS. A simple one step cerium conversion coating formation on to magnesium T alloy and electrochemical corrosion performance. *Surface and Coatings Technology*. 2018;349:757-772.

32. Sun J, Wang G. Preparation and characterization of a cerium conversion film on magnesium alloy. *Anti-Corrosion Methods and Materials*. 2015;62(4):253-258.

33. Maddela S, O'Keefe MJ, Wang YM, Kuo HH. Influence of surface pretreatment on coating morphology and corrosion performance of cerium- based conversion coatings on AZ91D alloy. *Corrosion Science*. 2010;66(11):115006-1-115006-8.

34. Maddela S, O'Keefe MJ, Wang YM. Effect of hydrogen peroxide concentration on corrosion resistance of cerium-based conversion coatings on Mg AZ91D alloy. *ECS Transactions*. 2012;41(15):13-26.

35. Bagalà P, Lamastra FR, Kaciulis S, Mezzi A, Montesperelli G. Ceria/stannate multilayer coatings on AZ91D Mg alloy. *Surface and Coatings Technology*. 2012;206(23):4855-4863.

36. Lee YL, Chu YR, Chen FJ, Lin CS. Mechanism of the formation of stannate and cerium conversion coatings on AZ91D magnesium alloys. *Applied Surface Science*. 2013;276:578-585.

37. Ferreira Junior M, Souza KP, Queiroz FM, Costa I, Tomachuk CR. Electrochemical and chemical characterization of electrodeposited zinc surface exposed to new surface treatments. *Surface and Coatings Technology*. 2016;294:36-46.

38. Stoychev D. Corrosion protective ability of electrodeposited ceria layers. *Journal of Solid State Electrochemistry*. 2013;17:497-509.

39. Guergova D, Stoyanova E, Stoychev D, Avramov I, Stefanov P. Self-healing effect of ceria electrodeposited thin films on stainless steel in aggressive 0.5 mol/L NaCl aqueous solution. *Journal of Rare Earths*. 2015;33(11):1212-1227.

40. Tougaard S. Surface nanostructure determination by x-ray phoemission spectroscopy peak shape analysis. *Journal of Vacuum Science and Technology*. 1996;14(3):1415-1423.

41. Montemor MF, Simões AM, Carmezim MJ. Characterization of rare-earth conversion films formed on the AZ31 magnesium alloy and its relation with corrosion protection. *Applied Surface Science*. 2007;253(16):6922-6931.

42. Brett CMA, Dias L, Trindade B, Fischer R, Mies S. Characterization by EIS of ternary Mg alloys synthesized by mechanical alloying. *Eletrochimica Acta*. 2006;51(8):1752-1760.

43. Fang D, Li X, Li H, Peng Q. Electrochemical corrosion behavior of backward extruded Mg-Zn-Ca alloys in different media. *International Journal of Electrochemical Science*. 2013;8:2551-2565.

44. Ba Z, Dong Q, Zhang X, Qiang X, Cai Z, Luo X. Cerium-based modification treatment of Mg-Al hydrotalcite film on AZ91D Mg alloy assisted with alternating electric field. *Journal of Alloys and Compounds*. 2017;695:106-113.

45. Gobara M, Shamekh M, Akid R. Improving the corrosion resistance of AZ91D magnesium alloy through reinforcement with titanium carbides and borides. *Journal of Magnesium and Alloys*. 2015;3(2):112-120.

46. Lin C, Changguo C, Ningning W, Jimin W, Ling D. Study of cerium and lanthanum conversion coatings on AZ63 magnesium alloy surface. *Rare Metal Materials and Engineering*. 2015;44(2):333-338.

47. Choi HY, Kim WJ. Development of the highly corrosion resistant AZ31 magnesium alloy by the addition of a trace amount of Ti. *Journal of Alloys and Compounds*. 2016;664:25-37.

48. Zucchi F, Grassi V, Frignani A, Monticelli C, Trabanelli G. Electrochemical behaviour of a magnesium alloy containing rare earth elements. *Journal of Applied Electrochemistry*. 2006;36:195-204.

49. Liu Y, Huang J, Claypool JB, Castano CE, O'Keefe MJ. Structure and corrosion behavior of sputter deposited cerium oxide based coatings with various thickness on Al 2024-T3 alloy substrates. *Applied Surface Science*. 2015;355:805-813.

50. Sonmez S, Aksakal B, Dikici B. Influence of hydroxyapatite coating thickness and powder particle size on corrosion performance of MA8M magnesium alloy. *Journal of Alloys and Compounds*. 2014;596:125-131.

Supplementary material

The following online material is available for this article:

Figure A1 - Representative XPS core level for the Ce3d region of the conversion film obtained after 20 s of immersion.

Figure A2 - Representative XPS core level for the O1s region of the conversion film obtained after 20 s of immersion.

Figure A3 - Representative XPS core level for the Ce3d region of the conversion film obtained after 120 s of immersion.

Figure A4 - Representative XPS core level for the O1s region of the conversion film obtained after 120 s of immersion.